

Figuring Out Gas & Galaxies in Enzo (FOGGIE). XV. Examining the Spatial and Kinematic Relationship between Circumgalactic Mg II and O VI

MACKENZIE TICORAS ^{1,2} BRIAN W. O'SHEA ,^{2,1,3,4} CLAIRE KOPENHAFER ,⁴ CASSANDRA LOCHHAAS ,^{5,6} MOLLY S. PEEPLES ,^{7,8} JASON TUMLINSON ,^{7,8} CAMERON TRAPP ,⁸ VIDA SAEEDZADEH ,⁸ RAMONA AUGUSTIN ,⁹ NICOLAS LEHNER ,¹⁰ BRITTON D. SMITH ,¹¹ AND J. CHRISTOPHER HOWK ,¹⁰

¹Department of Physics & Astronomy, 567 Wilson Road, Michigan State University, East Lansing, MI 48824

²Department of Computational Mathematics, Science, & Engineering, Michigan State University, 428 S. Shaw Lane, East Lansing, MI 48824

³Facility for Rare Isotope Beams, Michigan State University, East Lansing, MI 48824, USA

⁴Institute for Cyber-Enabled Research, 567 Wilson Road, Michigan State University, East Lansing, MI 48824

⁵Center for Astrophysics, Harvard & Smithsonian, 60 Garden St., Cambridge, MA 02138

⁶NASA Hubble Fellow

⁷Space Telescope Science Institute, 3700 San Martin Dr., Baltimore, MD 21218

⁸Center for Astrophysical Sciences, William H. Miller III Department of Physics & Astronomy, Johns Hopkins University, 3400 N. Charles Street, Baltimore, MD 21218

⁹Leibniz-Institut für Astrophysik Potsdam (AIP), An der Sternwarte 16, 14482 Potsdam, Germany

¹⁰Department of Physics and Astronomy, University of Notre Dame, Notre Dame, IN 46556

¹¹Institute for Astronomy, University of Edinburgh, Royal Observatory, EH9 3HJ, UK

ABSTRACT

Understanding the thermodynamic properties of the circumgalactic medium (CGM) is key to uncovering the baryon cycle in galaxies. Here we present spatial and kinematic relationships between Mg II and O VI as representatives for low and high ion-bearing gas, in the cosmological zoom-in galaxy simulation suite FOGGIE, a set of Milky-way-like galaxy simulations with high CGM resolution. We find the O VI-bearing gas exists as a diffuse halo around the galactic disk, while the Mg II-bearing gas is more centrally located. We investigate the covering fraction, probability of co-observation, co-kinematic correspondence of these ions using two different analysis methods. We make both mock sightlines using two-dimensional projections of our simulations treating these cells as integrated lines of sight and we create one-dimensional ray objects and use the SALSA (Boyd et al. 2020) code to investigate individual gas structures that contribute most to the line of sight column densities, which we call mock absorbers. We explore the relative kinematics of these mock absorbers and find Mg II and O VI appear to have a co-kinematic relationship when looking at absorber pairs with the closest relative velocity like in Werk et al. (2016). However, this does not necessarily correspond with a close spatial separation meaning many O VI and Mg II absorber pairs only appear to be co-kinematic but are physically unrelated. Taking a more holistic look at Mg II and O VI absorber pairs reveals a much weaker correlation between these two ions.

Keywords: Circumgalactic medium (1879)—Hydrodynamical simulations (767)

1. INTRODUCTION

The circumgalactic medium (CGM) is a vast multi-phase and ionized plasma surrounding a galaxy, which is thought to contain a significant fraction of a galaxy's to-

tal baryons (Werk et al. 2014; Lehner et al. 2015; Stocke et al. 2013). Baryons move through the CGM exchanging with the galaxy disk and intergalactic medium in what is normally termed the “baryon cycle” (see, e.g., Péroux & Howk 2020). This cycle implicitly controls the amount of material in different galactic reservoirs (stars, interstellar medium, intergalactic medium, etc.) affecting key properties of a galaxy like star formation rate,

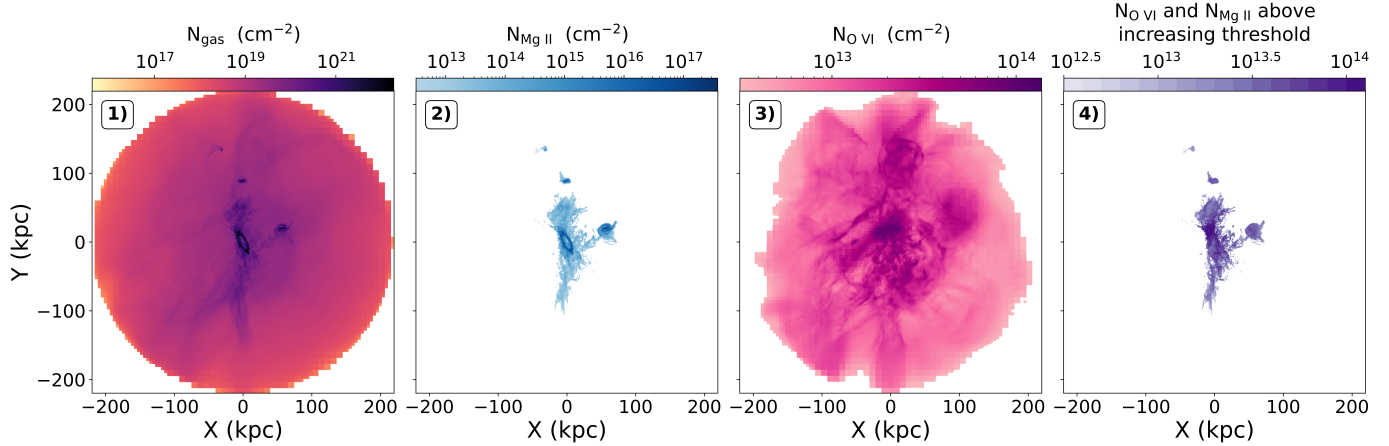


Figure 1. All four panels show a projection of one of the FOGGIE galaxies (Blizzard) at $z = 0$. Left to right: 1) A projection of total gas density, represented as a column density in cm^{-2} . 2) A projection of Mg II column density with only column densities greater than the threshold of $N = 10^{12.5} \text{ cm}^{-2}$ shown. 3) A projection of O VI column density with only column densities greater than the threshold of $N = 10^{12.5} \text{ cm}^{-2}$ shown. 4) The observable column density threshold is incremented between $10^{12.5} \text{ cm}^{-2} < N < 10^{14.1} \text{ cm}^{-2}$, which marks the highest column density for O VI in the dataset. The pixels are colored by whether the Mg II and O VI column densities are both above the threshold listed in the colorbar.

metallicity, etc. Therefore, understanding the structure and dynamics of the material in the CGM is critical to understanding galaxy dynamics on many scales.

A key way we can probe the thermodynamic structure of the CGM is through ionic column density measurements from absorption spectra. The measurements take place by looking at the light from quasi-stellar objects (QSOs) that passes through the CGM of a galaxy. Light absorption occurs at certain wavelengths depending on the atomic and ion composition of the plasma. These absorption features are detectable in spectra and the ion composition reveals the thermodynamic properties of the medium. Measuring these features in spectra is a key way that we can determine the density and temperature of the CGM. Study of the CGM through ion column densities often occurs in population studies (e.g., [Chen et al. 2010](#); [Werk et al. 2016](#); [Lehner et al. 2022](#)), which can give us insight into the general properties of galaxies over a range of system masses. However, surveys of Andromeda and our own Milky Way CGM are also possible, allowing us to get a more detailed picture of an individual galaxy system (e.g., [Fox et al. 2020](#); [Qu et al. 2024](#); [Lehner et al. 2015, 2020, 2025](#)). Although limited, these types of observations can tell us about the temperature, density, and composition of the CGM as well as the kinematic structure of the gas.

We often break our collection of ion features into groups. Neutral or weakly ionized atoms (e.g., Si I, Mg II) tend to inhabit colder, more dense regions of gas, whereas highly ionized atoms (C IV, O VI, etc.) tend

to inhabit hotter, less dense regions of gas (see Figure 6 in [Tumlinson et al. \(2017\)](#) for more details). Here, we refer to these two groups as “low ions” and “high ions.” A broad range of both low and high ions are often measured in a single observational sightline and it is valuable to investigate the conditions that lead to the detection of multiple gas phases. This work uses Mg II and O VI to represent the low ion and high ion categories, respectively. We choose these two ions because they have strong oscillator strength ([Tumlinson et al. 2017](#)) and often appear in CGM observations (e.g., [Cherrey et al. 2025](#); [Chen et al. 2010, 2025](#); [Ho et al. 2025](#); [Sameer et al. 2024](#); [Dutta et al. 2025](#)).

In general, we are also interested in the relative kinematics of ions. The line-of-sight velocity of absorption features is a quantity we can measure by looking at the wavelength offset from rest-frame absorption — after correcting for the redshift of the host galaxy. Absorbers often have several components, which indicate absorption from multiple distinct structures in the CGM. It has been suggested in observations (e.g. [Werk et al. 2016](#); [Tripp et al. 2008](#)) that the line-of-sight velocity components of O VI aligns closely with those of low ions. This would indicate that that O VI is co-moving with low ions. This is a non-intuitive finding since these ions occupy substantially different temperature and density phase spaces and should be uncorrelated with one another. However, this is a complicated problem because the velocity of O VI absorbers vary widely ([Lehner et al. 2014](#)) and are usually broad ([Werk et al. 2016](#)). We

largely complete our analysis through the lens of Werk et al. (2016) using specifically Mg II as our tracer for low ion-bearing gas and we directly compare to results from that paper.

This paper traces Mg II and O VI in the high-resolution FOGGIE simulations, which are a suite of Milky-Way like galaxy simulations with forced high resolution for much of the circumgalactic region (for more details on the simulations, see Section 2). Numerical simulations like these are valuable as they allow us to probe our models and hypotheses surrounding galaxies. Since we are often limited in the data that can be obtained on individual galaxies (i.e., it is typical to have one QSO sightline through a galaxy), simulations allow us to synthesize observational population statistics and theoretical models to attempt to imitate a galaxy and its CGM. The main focus of our investigation is to examine the spatial and kinematic relationship between cool and warm gas, as traced by Mg II and O VI, in the FOGGIE simulations and compare these results to observations.

Section 2 outlines the characteristics of the simulations. Section 3 discusses the spatial properties of the Mg II and O VI-bearing gas with mock sightlines created by projecting the simulations into two dimensions. Section 4 examines the spatial structure and kinematics of individual absorbers that are computed via the SALSA package (Boyd et al. 2020), which picks out these absorbers from one-dimensional ray objects that model observational sightlines. Section 5 investigates insights we gain by comparing the results of Section 3 and Section 4, connects the results of previous sections with observations data, and discusses limitations and caveats of this work. Finally, Section 6 summarizes the results and key points of this paper.

2. SIMULATIONS AND METHODS

We outline details of the “Figuring out Gas & Galaxies in Enzo” (FOGGIE) simulations that we use for this paper in Section 2.1. We then describe how we obtain the ionization fractions on a cell-by-cell basis in Section 2.2.

2.1. The FOGGIE Simulations

We use the FOGGIE simulations, first introduced in Peebles et al. (2019). For these simulations, an initial, cosmological simulation of size $100 h^{-1}$ comoving Mpc was generated at low resolution using ENZO — a hydrodynamical adaptive mesh refinement code (Bryan et al. 2014; Brummel-Smith et al. 2019). These initial simulations were generated using a flat Λ CDM model of the universe with $1 - \Omega_\Lambda = \Omega_m = 0.285$, $\Omega_{\text{baryon}} = 0.00461$, and $h = 0.695$. From this, six halos were identified

(Tempest, Squall, Maelstrom, Blizzard, Hurricane, and Cyclone) with Simons et al. (2020) being the first paper to discuss the properties of these six halos. Additional details about these FOGGIE halos can be found in Simons et al. (2020) and Wright et al. (2024).

We have selected these six halos such that at $z = 0$ they are Milky Way-mass (between $M_{\text{vir}} \approx (0.5 - 1.5) \times 10^{12} M_\odot$) and have no major mergers (defined as a mass ratio of 10:1 or lower) after $z = 2$, which mirrors the believed last major merger of the Milky Way (Helmi et al. 2018). After identifying these halos the simulations were re-run starting at $z = 100$ with much greater mass resolution around these halos. The unique aspect of the FOGGIE simulations starts at $z = 6$ where we implement a “forced refinement” box. The forced refinement box extends $\pm 100 h^{-1}$ comoving kpc from the galaxy center and everything within the forced refinement box is refined to at least ~ 1 comoving kpc with the highest refinement being 274 comoving pc. This allows us to obtain high spatial resolution for gas extending out to a significant fraction of the virial radius. It has previously been shown that simulation resolution can greatly affect the simulated gas distribution in the CGM (Peeples et al. 2019; Corlies et al. 2020; van de Voort et al. 2019; Hummels et al. 2019; Suresh et al. 2019), so modeling with high resolution is key to modeling the CGM accurately — particularly in regions normally associated with warm/hot CGM gas, which is often less resolved than cooler, denser parts of the galaxy.

These simulations implement metallicity-dependent radiative cooling and chemistry through Grackle (Smith et al. 2017) with redshift-dependent UV backgrounds following Haardt & Madau (2012) that include self-shielding. We model star formation and thermal feedback following the methods of Cen & Ostriker (1992, 2006) with small changes following Smith et al. (2011) to better distribute thermal energy deposited by feedback. These simulations create star particles with a minimum mass of $\sim 10^3 M_\odot$, depending on redshift. The FOGGIE simulations do not include a method for AGN feedback.

2.2. Extracting Ionization

In the FOGGIE simulations the metallicity is tracked as a single field, but for this analysis we are interested into decomposing the metallicity into specific ionization states. We use Trident (Hummels et al. 2017) to add ion concentrations on a cell-by-cell basis. Trident calculates ion fractions by interpolating between values in the CLOUDY (Ferland et al. 2013) tables. The ion fractions are based on the temperature, density, and redshift

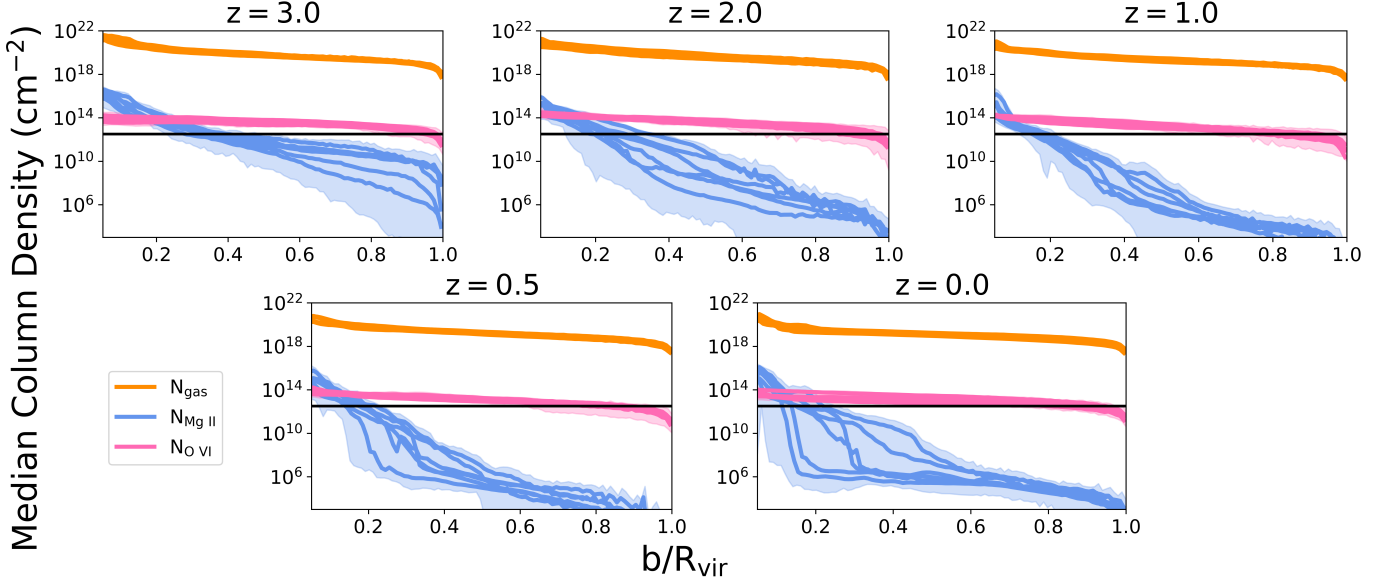


Figure 2. Median column density versus impact parameter for the two-dimensional mock sightline datasets at redshifts $z = 3, 2, 1, 0.5$, and 0 . We have normalized our impact parameter, b , by the virial radius, R_{vir} . The orange lines represent the total gas column density, the blue line represents the Mg II column density, and the pink line represents the O VI column density. Each line is the average across 10 orientations (the x , y , and z axes of the simulation and 7 random orientations) for each of the six FOGGIE halos. The shaded regions represent the absolute maximum and minimum across all orientations and all halos. The horizontal black line is at $N = 10^{12.5} \text{ cm}^{-2}$ which represents the observable threshold that we choose for this analysis.

of the cell. These tables assume Solar abundances and assume a UV background following Haardt & Madau (2012). More specifically, we consider the self-shielding versions of these tables from Emerick et al. (2019), which include self-shielding by integrating to a depth into the cloud equivalent to the local Jeans length or a maximum of 100 pc.

3. MOCK SIGHTLINES IN PROJECTED GRIDS

For this section, we construct datasets of mock sightlines for single redshift snapshots of the FOGGIE simulations. We consider only cells between $0.05 R_{\text{vir}}$ and R_{vir} for each halo at each redshift (We consider redshifts of $z = 3, 2, 1, 0.5$ and 0). This gives us just material inside the CGM and cuts out material from the galactic disk and intergalactic medium. We project the three-dimensional FOGGIE simulation snapshots along a single axis only including the material between our range of $0.05 R_{\text{vir}} - R_{\text{vir}}$ in our projections. The result is a two-dimensional dataset upon which we impose a uniform grid of 800 by 800 cells. These cells act as our mock sightlines, which imitate QSO absorption spectroscopy as they contain information integrated along line-of-sight for our defined CGM region. From this grid of mock sightlines we extract column density. This whole process is repeated for 10 different orientations (the x , y , and z axes of the simulation and 7 random orientations). We take the average across these orienta-

tions for Figures 2, 3, and 4 to limit the effect that viewing angle has on our results.

We choose a threshold of $N = 10^{12.5} \text{ cm}^{-2}$ for Mg II and O VI column densities, which we consider to be approximately “observable” column densities of these ions (Tumlinson et al. 2017), so we can discuss our results in terms of the observational limits. We choose Mg II and O VI to represent low-ion-bearing and high-ion-bearing gas (or cool and warm temperature gas), respectively. These ions are often detected in spectra of the CGM of Milky Way-like galaxies. The complications associated with column densities observationally and the limits of setting specific threshold are discussed in Section 5.

Section 3.1 discusses radial profiles of the Mg II and O VI column densities. Section 3.2 will discuss the probability of our sightlines containing Mg II and O VI column being above the threshold and how this probability changes as a function of impact parameter.

3.1. Projected Radial Distribution of Mg II and O VI

Figure 1 shows a visual representation of these two-dimensional datasets of mock sightlines. The first three panels show the total, Mg II, and O VI column density in a two-dimensional projection of the FOGGIE galaxy “Blizzard” at $z = 0$. The fourth panel shows a map of the overlap between Mg II and O VI column densities as we incrementally increase the “observability threshold” from $12.5 \leq \log_{10} N \leq 14.1$. This shows us where

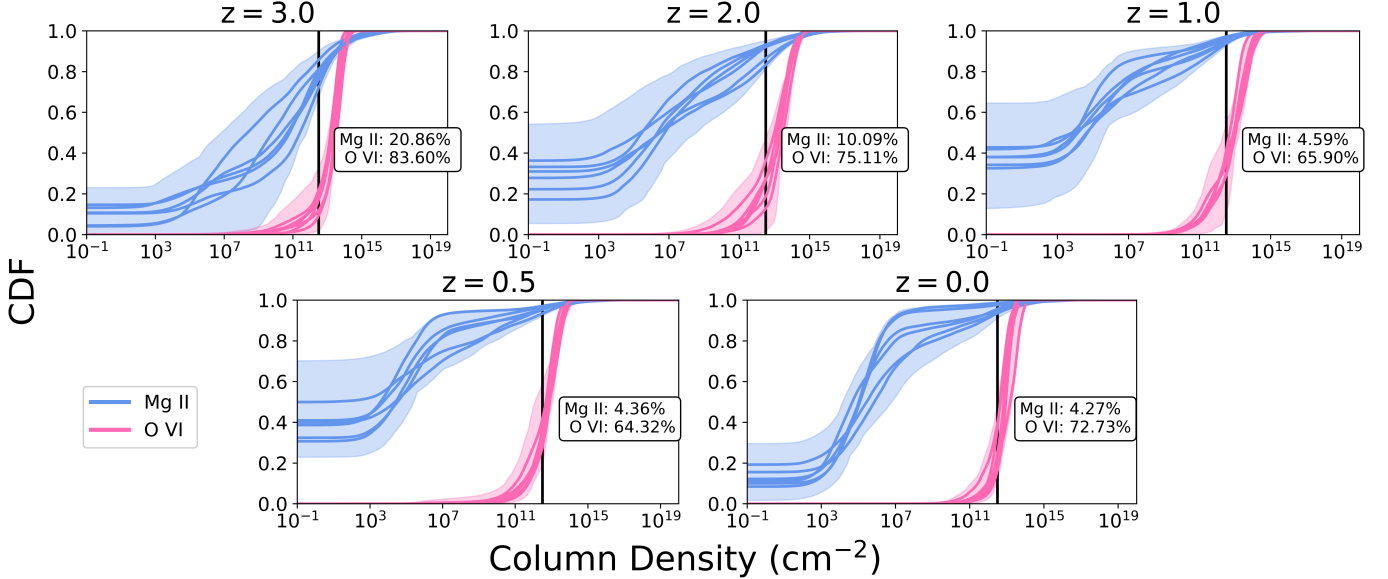


Figure 3. Cumulative distribution functions (CDF) of Mg II (blue) and O VI (pink) column density values. The black vertical line represents our observable threshold of $N = 10^{12.5} \text{ cm}^{-2}$. As an annotation, we report the percent of mock sightlines that contain Mg II and O VI column densities above the threshold as averaged across all of six FOGGIE halos at each redshift. Each line represents the average across 10 orientations for a FOGGIE halo and the shaded regions represent the absolute maximum and minimum across all orientations for all halos. We report these distributions at redshifts of $z = 3, 2, 1, 0.5$, and 0.

there are large concentrations of both ion column densities. We can see in Panel 2 that Mg II column densities above the threshold tend to be close to the galactic center, whereas O VI column densities above the threshold in Panel 3 tend to be more uniformly distributed within the virial radius. Additionally, Panel 4 shows that the overlap between observable column densities of Mg II and O VI is mostly constrained by the location of observable Mg II sightlines. This demonstrates that observable sightlines of O VI should be very common at most impact parameters.

In Figure 2, we quantify this phenomenon with radial profiles of our two-dimensional datasets exploring the median of the total gas, Mg II, and O VI column densities. Each line represents the median values over 10 different orientations (the x, y, and z axes of the simulation and 7 random orientations) for each FOGGIE halo. The shaded region behind the Mg II and O VI column density profiles represents the absolute maximum and minimum found across all galaxies and orientations. The black horizontal line denotes our observable threshold at $N = 10^{12.5} \text{ cm}^{-2}$. We see in this figure that the column density radial profile of Mg II starts higher than the O VI profile, but drops below the observable threshold at around $(0.2 - 0.3)R_{\text{vir}}$. The median O VI column density is flat, however, remaining around $N \sim 10^{13} - 10^{14} \text{ cm}^{-2}$ out to nearly the virial radius. These trends hold across all six FOGGIE halos.

It is important to note for Figure 2 that the virial radius is not constant across the halos or across time. The halos have inherently different sizes and range in $z = 0$ mass between $M_{\text{vir}} \approx (0.5 - 1.5) \times 10^{12} M_{\odot}$. This results in a range of virial radii between 16–43 kpc at $z = 3$ which increase over time to 170–252 kpc at $z = 0$.

All of the halos have a fairly tight agreement for column density values in the profiles, especially for O VI column densities and the total column density. There appears to be more scatter in the Mg II column density, which could mean that Mg II is not equally distributed throughout the CGM but is preferentially aligned along a direction, potentially with the galactic disk. There is also little difference between each radial profile across redshift. The total and O VI column densities maintain similar values and shape across redshift. The Mg II profiles appear to drop off more sharply at low redshift than they do at high redshift with the normalized impact parameter. However, it is important to note that the virial radius increasing is a contributing factor and the absolute size of the Mg II distribution stays closer to constant over time in absolute distance.

3.2. Probability of column densities above the threshold

Only a fraction of mock sightlines contain a column density above the $N = 10^{12.5} \text{ cm}^{-2}$ threshold in each two dimensional dataset. The probability of a mock sightline having Mg II or O VI column density above the threshold is quantified in Figure 3. This figure shows the cumulative distribution functions (CDF) over the

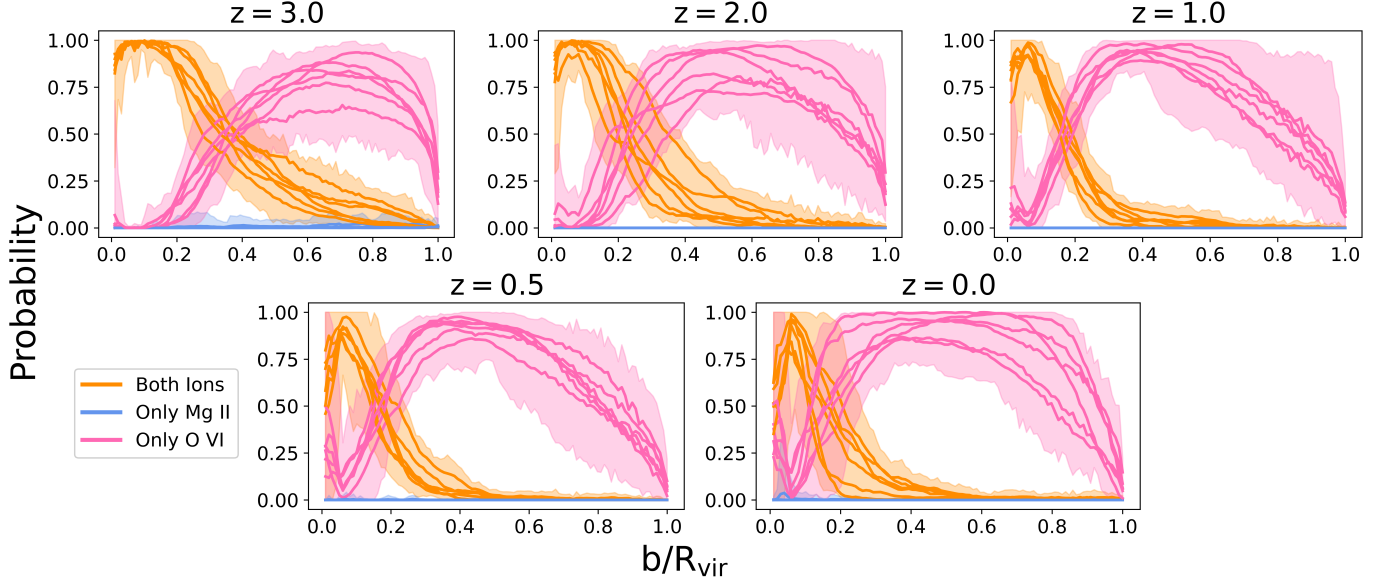


Figure 4. Probability of a projected mock sightline containing column densities of only Mg II, only O VI, or both above the threshold of $N = 10^{12.5} \text{ cm}^{-2}$ as a function of impact parameter. The orange represents the probability of both being observed, the blue represents the probability of only Mg II being above the threshold and the pink represents the probability of only O VI being above the threshold. Each line represents the average across 10 orientations for a FOGGIE halo and the shaded regions represent the absolute maximum and minimum across all orientations for all halos. We report these distributions at redshifts of $z = 3, 2, 1, 0.5$, and 0 .

column densities of both Mg II and O VI where the black line is again our observable threshold. We can use these datasets to imitate covering fraction since these sightlines are uniformly distributed throughout the entire two dimensional virial radius. The observable covering fraction for Mg II column densities is around 5 – 10%, whereas the observable O VI column densities covering fraction is closer to 65 – 80%. The average percentage above the threshold across the FOGGIE galaxies is reported for each redshift in each subplot of Figure 3. The result is that a random sightline within the virial radius is much more likely to contain an observable column density of O VI than Mg II.

There is a small but noticeable difference in the probability of Mg II column densities falling above the threshold as a function of redshift. At higher redshifts, we see a greater percentage of mock sightlines that have Mg II above the threshold. This is likely because the halos have smaller virial radii and cool gas extends farther out as the galaxy’s disk is still forming.

Figure 3 examines all mock sightlines within the virial radius equally; however, as we could deduce from the structure seen in Figure 2, these probabilities are dependent upon impact parameter. Figure 4 shows the probability of mock sightlines containing column densities of just Mg II, just O VI, or both above the observable threshold. We can see at low impact parameter we have a high probability of a mock sightline containing both

Mg II and O VI, but around $(0.3 – 0.5)R_{\text{vir}}$ (depending on halo/redshift), the probability of observing both dips down to roughly zero. The majority of mock sightlines begin to contain just O VI column densities above the threshold and not Mg II column densities above the threshold. This result is consistent with trends seen in Figures 1 and 2 where there are few, if any, Mg II column densities above the threshold at larger impact parameters. At large impact parameter all of the lines move towards zero, meaning that there are many sightlines that do not contain observable column densities of either Mg II or O VI.

The key takeaway from of Figure 4 is that for low impact parameters ($\lesssim 0.3R_{\text{vir}}$) we would expect to observe both Mg II and O VI along a line of sight, and at mid to high impact parameters, we would only expect to observe O VI. We would almost never expect to have a column density of Mg II above the threshold without there also being a column density of O VI above the threshold. This is true across all halos and redshifts.

4. MOCK ABSORPTION FEATURES ALONG SIGHTLINES

We investigate the physical structures of gas along a sightline so we can compare how specific clumps or overdensities of gas interact with each other. We identify these overdensities using the software package SALSA, Synthetic Absorption Line Surveyor Application (Boyd et al. 2020). SALSA identifies physically and kinemat-

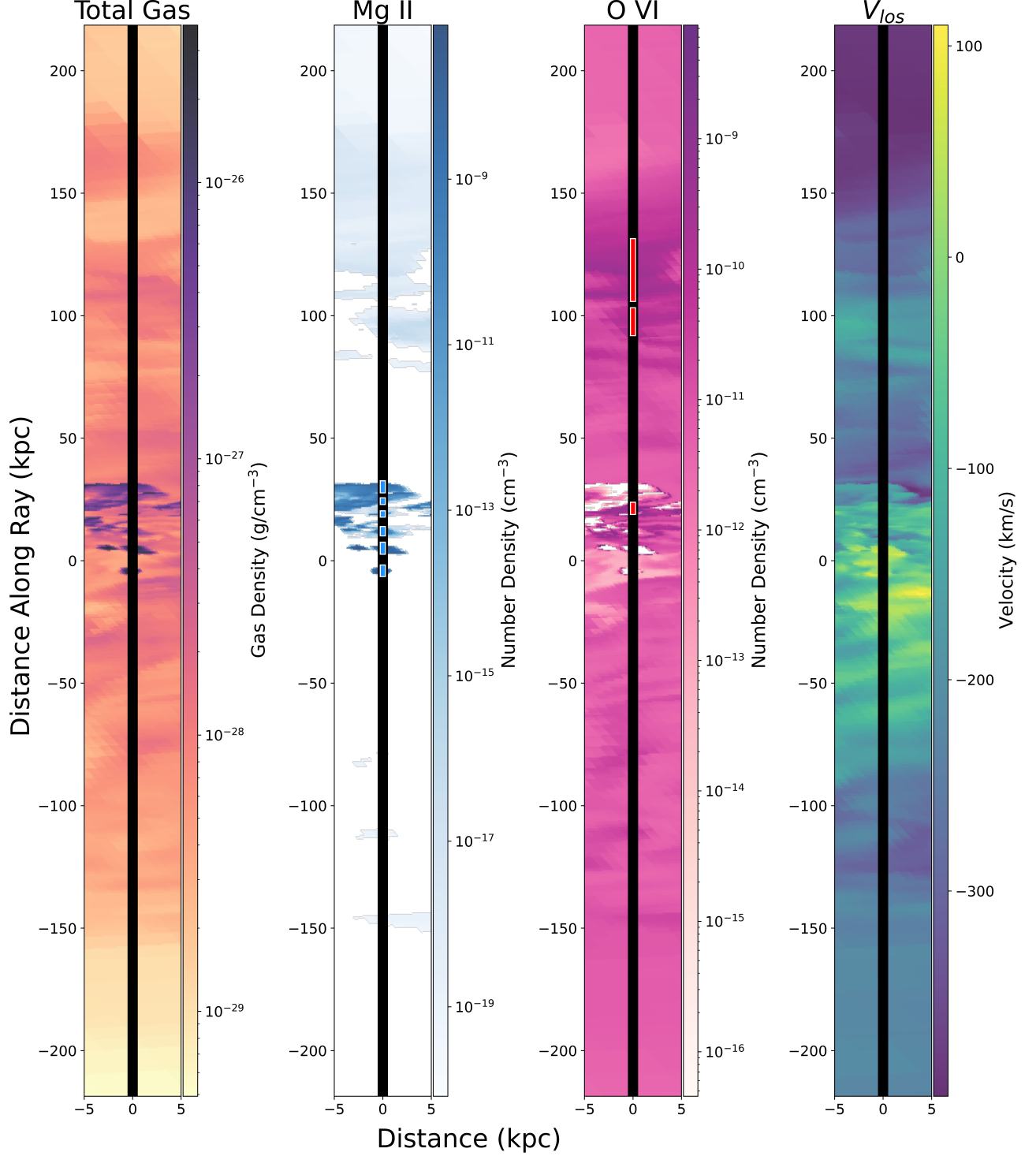


Figure 5. Two-dimensional slice plots through the FOGGIE galaxy Blizzard at $z = 0$ aligned with a one-dimensional SALSA ray that passes through the dataset (marked as the black vertical line through $x = 0$). All four images from left to right show the same ray with slices in the total gas density, Mg II number density, O VI number density and line-of-sight velocity ($\vec{v} \cdot \hat{r}$). A perpendicular distance of ± 5 kpc is chosen arbitrarily to show the gas structures that the one-dimensional ray passes through. The short blue and red lines drawn on top of the black ray line in the Mg II and O VI number density plots represent locations of the mock absorbers detected by SALSA. This ray, like all other rays in the dataset, passes through the entire virial radius, and only contains information from within the virial radius. This ray passes through the galaxy at an impact parameter of 20.7 kpc.

ically contiguous overdensities of individual ion column densities along a one dimensional ray through the simulation. All of these absorbers achieve a column density greater than $N = 10^{12.5} \text{ cm}^{-2}$. It compiles these overdensities into a set of mock absorbers for that ray (specifics on how SALSA identifies mock absorbers can be found in Appendix A). For this paper, we use the SPICE algorithm in the SALSA package to identify mock absorbers.

At each redshift for each halo we construct 400 one-dimensional rays with SALSA at random orientations and with impact parameters between 5–40% the virial radius. We extract the Mg II and O VI mock absorbers from these rays. Figure 5 gives a visual representation of just one of these rays in gas density, Mg II density, O VI density, and line of sight velocity. The black line in these images is the one-dimensional trajectory of the SALSA ray and a slice, or two-dimensional plane, is rendered around the ray to demonstrate the properties of the plasma that the ray is passing through. The red and blue lines on top of the black lines are the Mg II and O VI absorbers that SALSA picks out for this ray. We use this figure as an intuition-building example to guide the reader’s understanding for how the dataset used in this section is constructed.

Section 4.1 will discuss the probability of a ray containing just O VI mock absorbers, just Mg II mock absorbers, or both versus impact parameter. Section 4.2 will discuss the difference and distance and line of sight velocity of pairs of Mg II and O VI mock absorbers.

4.1. Absorber Detection Probabilities

Similar to Figure 4, we can look at the “observable probability” vs. impact parameter. However, the method and meaning behind this calculation in Figure 6 is different than Figure 4. Before, with the two-dimensional mock sightline images the threshold of $N = 10^{12.5} \text{ cm}^{-2}$ applied to the total integrated column density over the whole ray. SALSA works differently, identifying physically distinct over-dense “clumps” of specific ion along the line of sight that would likely make up a single and distinct absorption feature. Each one-dimensional clump must have a total column density greater than $N = 10^{12.5} \text{ cm}^{-2}$ to be identified. Both methods produce similar trends on a broad scale, but we discuss the differences between these two methods and what this indicates about the results in Section 5.3. Here we focus on just the results from the SALSA analysis itself.

We see in Figure 6 that at low impact parameter we have a high probability of both Mg II and O VI absorbers being identified in the ray. This gradually drops

off with impact parameter and at large impact parameters we expect to see mostly O VI absorbers alone in the rays. This is largely fueled by the central nature of the Mg II-bearing gas, as previously discussed. There is a slightly greater chance of picking out Mg II absorbers in a ray without picking up O VI absorbers at low impact parameter than there was in Section 3, particularly at low redshift.

There is also some redshift dependence. We can see that as redshift decreases the probability of observing both Mg II and O VI absorbers reaches nearly zero at a lower impact parameter than it did with the analysis in Section 3. At $z = 0$ we reach approximately zero probability of observing both ions around $(0.15 - 0.25)R_{\text{vir}}$, whereas in Figure 4 we reach this over a range of $(0.2 - 0.4)R_{\text{vir}}$. Overall, this trend is due to the Mg II-bearing gas becoming more and more centrally located as the galaxy settles into its isolated state.

4.2. Spatial and kinematic relationships between absorbers

We can explore the kinematic relationship between pairs of mock absorbers by looking at difference in line-of-sight velocity that occurs between Mg II and O VI mock absorbers. Figure 7 shows the relationship between the difference in column density weighted average line-of-sight velocity and the difference in line-of-sight distance between Mg II and O VI absorber pairs. Absorber pairs are limited to Mg II and O VI mock absorbers along the same ray since we aim to model QSO sightlines through the CGM. However, if multiple Mg II and O VI absorbers occur along a ray, all combinations of Mg II and O VI pairs are considered. The number of absorber pairs that occur along our mock sightlines vary, but we keep consistent the total number of rays at each redshift for each halo at 400. All of the halos are combined to make each subplot in Figure 7 as the structure and distribution of these ions across all of the previous figures show that they are in remarkable agreement. SALSA keeps track of the physical extent of each mock absorber along the ray and we compare the geometric midpoints (average of the of start and end points) of these mock absorbers to get the relative distance between mock absorber pairs.

We can see in Figure 7 that there are a wide range in velocity differences and distance difference between the mock absorber pairs. It is important to note that the distance at higher redshift cannot extend as high as lower redshift since we limit that data to within the virial radius, and the virial radii are smaller at high redshift. There is a “hot zone” at low velocity and distance difference, but the black median line and blue 80th percentile

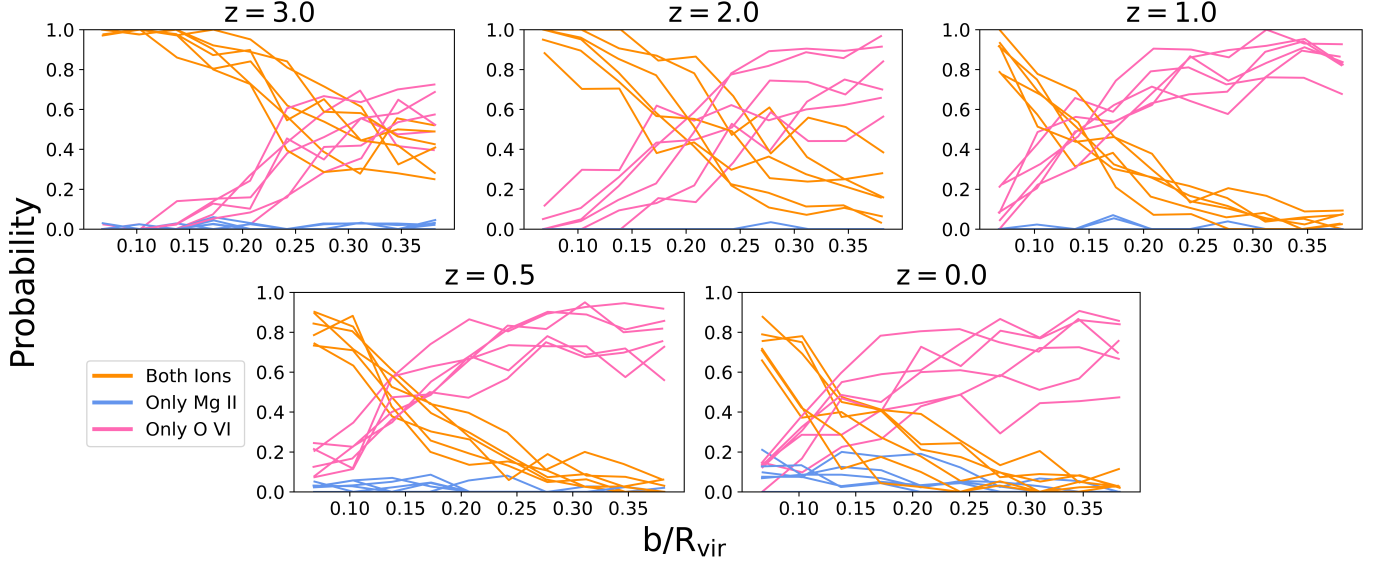


Figure 6. The probability of detecting just Mg II mock absorbers, just O VI mock absorbers, or both mock absorbers within a ray as a function of impact parameter. The orange represents the probability of a ray having both mock absorbers, the blue represents the probability a ray having only Mg II mock absorbers and the pink represents the probability of a ray having only O VI mock absorbers. Each line for each color represents one of the six FOGGIE halos. All mock absorbers identified by SALSA are inherently above our threshold of $N = 10^{12.5} \text{ cm}^{-2}$. We report these distributions at redshifts of $z = 3, 2, 1, 0.5$, and 0 .

line show that the data is fairly spread out in velocity space, especially compared to the Werk et al. (2016) results shown as the vertical red line. Although the most populated bins of the two-dimensional histogram have low distance difference and low velocity difference, we can see that for a large population of absorber pairs we would expect the median of both the distance differences and velocity differences to be pulled further out by a trailing tail of larger and larger differences in both directions. Overall, this would suggest that these two ions, while having some correlation, are not as correlated in the FOGGIE simulations as we see in the COS-Halos QSO absorption line observations of Werk et al. (2016). This is discussed in more depth in Section 5.2.

5. DISCUSSION

This section furthers the discussion of our results, comparing to observations, considering the differences between analysis methods, and examining the caveats of our analysis. Section 5.1 compares the bulk distribution we see for Mg II and O VI column densities to observations. Section 5.2 discusses the spatial and kinematic relationship between Mg II and O VI absorbers, connecting our results to relevant observations. Section 5.3 examines the additional information we can gain by comparing our analyses from Section 3 and Section 4. Finally, Section 5.4 outlines some of the caveats of the results and analysis of this paper.

5.1. Distribution of Mg II and O VI-bearing gas

It is clear from the results in Figures 2, 3, and 4 that observable amounts of Mg II column density (greater than $N = 10^{12.5} \text{ cm}^{-2}$) occupy only a small covering fraction inside of the virial radius. Mg II-bearing gas exists mostly in the central regions around the galaxy, whereas the O VI-bearing gas exists as a significant, space-filling diffuse halo out to larger impact parameters. This is consistent with previous observations of gas distribution in Milky Way-like galaxies from population studies. Figure 2 in Tumlinson et al. (2017) shows this radial profile for many different ions across multiple population studies and Lehner et al. (2025) shows a detailed example for a single galaxy, Andromeda. We see very clearly that low ions (i.e., ions tracing cool gas) drop off more steeply in impact parameter than high ions (i.e., ions tracing gas with temperatures closer to the virial temperature).

This diffuse cloud of O VI-bearing gas would yield broader line widths due to the Doppler broadening given

$$\lambda_{obs} = \lambda_0 \left(1 + \frac{v_{gas}}{c} \right) \quad (1)$$

If we assume a rest frame wavelength of $\sim 1000 \text{ \AA}$ (appropriate for O VI) and a maximum velocity spread of roughly $v_{gas} \sim 10^3 \text{ km/s}$ (typical for a Milky-Way like galaxy) we would expect a broadening of a few \AA due to this halo structure. We do see in observations of O VI that it tends to have a more broad profile (Werk et al. 2016; Qu et al. 2024).

5.2. Relationship between Mg II and O VI absorbers

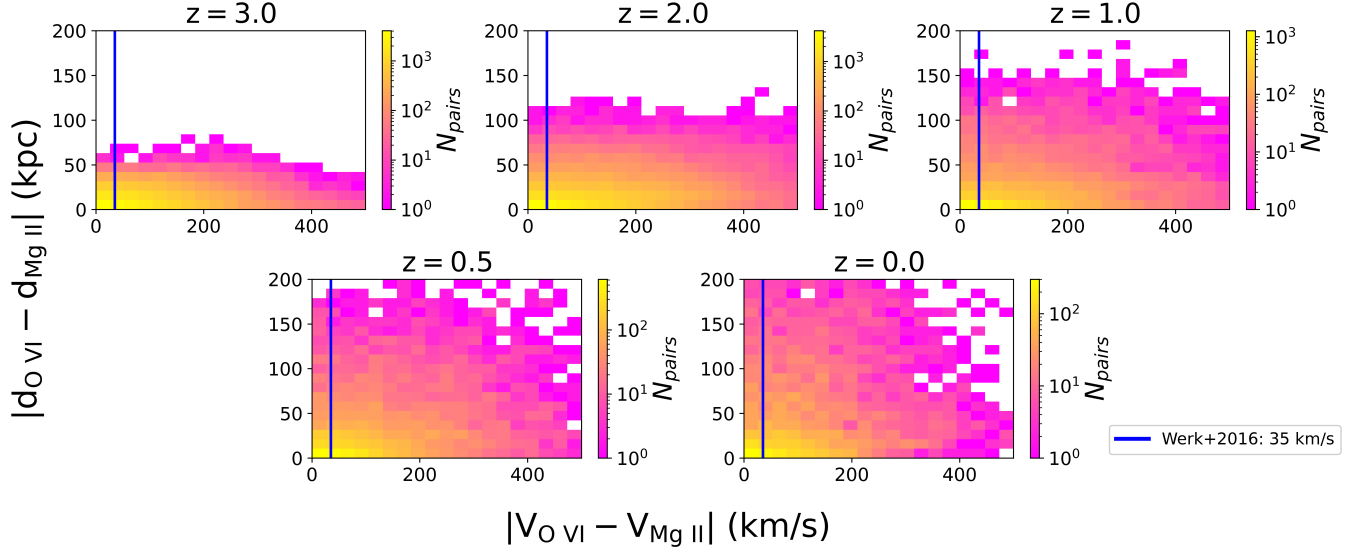


Figure 7. Two-dimensional histogram of the distance between pairs of Mg II and O VI mock absorbers and the column density weighted average line-of-sight velocity of these mock absorber pairs. All pairs are limited to the same ray, but if a single ray contains multiple Mg II and O VI mock absorbers all pairs of absorbers are considered. The color represents the number of absorber pairs that fall within the binned range. The blue vertical line represents 80% of O VI absorbers being within 35 km/s of a low ion absorber from Werk et al. (2016). Each panel contains mock absorber pairs from all six FOGGIE halos. We report these distributions at redshifts of $z = 3, 2, 1, 0.5$, and 0 . Note the distance difference is limited to $2R_{\text{vir}}$, and since virial radii are smaller at larger redshift we see a distance cutoff in the high redshift distributions.

There is a kinematic correspondence between O VI and low ions in observations even though based on the density and temperature phases these ions exist at we would not naively expect this (e.g., Werk et al. 2016; Tripp et al. 2008). These observations implicitly suggest a connection between high ion and low ion absorbers that could illuminate the structure of the circumgalactic gas. In Figure 8 we probe this relationship with four different cumulative distribution functions examining the co-kinematic structure of O VI and Mg II mock absorbers in our SALSA sightlines. The pink line considers all Mg II and O VI pairs at or above the threshold column density. The orange line considers only the physically closest absorbers along each ray. The purple line represents only the single largest column density pairing along each ray and the red line represents the absorber pair with the smallest velocity difference along the line of sight. The blue vertical line is at 35 km/s, which comes from Werk et al. (2016) where approximately 80% of O VI absorbers had a low ion absorber within 35 km/s. The red line is broadly consistent with the majority of the O VI mock absorbers having a Mg II mock absorber within ~ 35 km/s, and is most consistent with the comparison methodology used in Werk et al. (2016). However, the physically closest Mg II and O VI absorbers (as shown in orange in Figure 8) tend to have much larger velocity separations. This continues to be true for the largest column density pairing and all of the pairings in

the sightlines. This indicates that high velocity coincidence of between single O VI and Mg II absorbers along sightlines does not necessarily mean high spatial coincidence of these absorbers. Since most rays have multiple mock absorbers of each ion, we are seeing selection effect where absorbers that are in no way physically related appear to be co-kinematic. This may also be true for observations of these ions and seems to more closely align with the intuition that these ions trace different thermodynamic phases of gas and therefore should not generally be co-spatial.

5.3. Differences between Integrated Column Density Analysis and Absorption Feature Analysis

Both of the methods discussed in Sections 3 and 4 are typical ways that one can analyze simulations to more easily compare them to observations. The mock sightlines in Section 3 are integrated over the entire line of sight and are identified as “observable” if the column density exceeds $N = 10^{12.5} \text{ cm}^{-2}$. The mock sightlines in Section 4 are characterized only by individual absorbers along the line of sight, where absorbers must be physically continuous and have a smooth velocity gradient. Looking at the results of these two methods together, we can deduce the properties that diffuse gas plays in column density measurements. This diffuse gas contributes to the integrated lines of sight, but would not be identified as part of a physical absorber in Sec-

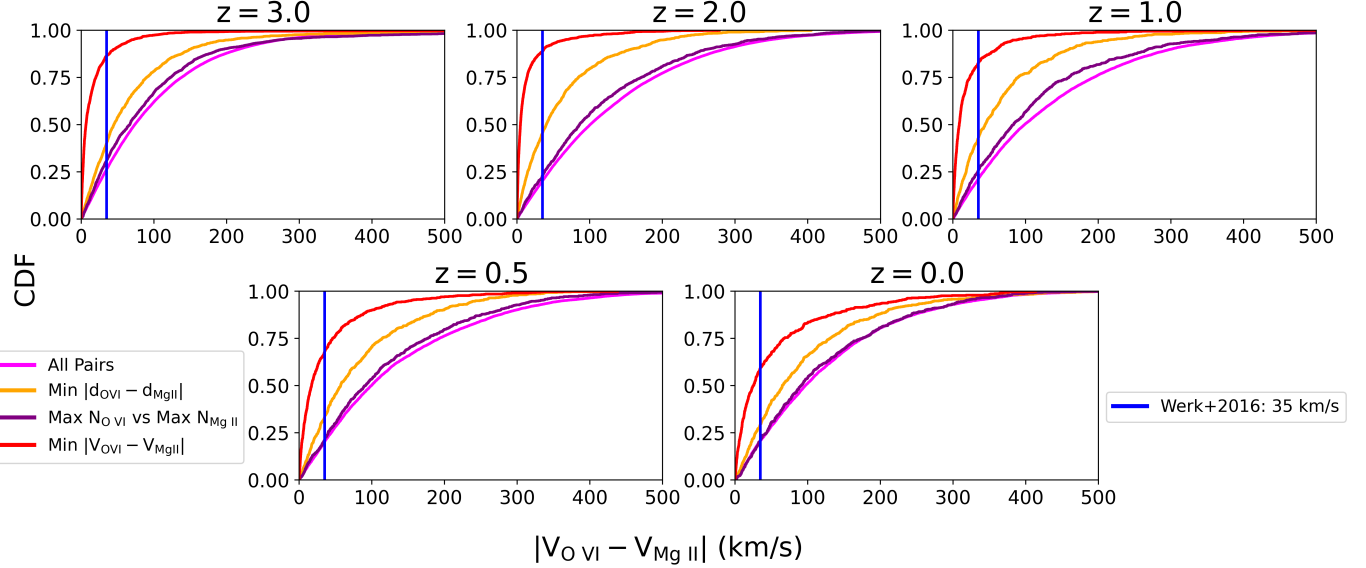


Figure 8. Cumulative distribution functions (CDF) of velocity difference between Mg II and O VI mock absorber pairs. The blue vertical line represents the 80% of O VI absorbers being within 35 km/s of a low ion absorber. We consider 4 different “cutoffs” for our CDFs: we look at the velocity difference between all pairs of Mg II and O VI mock absorbers (pink), only the closest pairs within a ray (orange), the single largest column density pair of Mg II and O VI mock absorbers along the sightline (purple), and the mock absorbers pair with the smallest velocity separation between them (red). We report these distributions at redshifts of $z = 3, 2, 1, 0.5$, and 0.

tion 4. We can see a comparison of these two methods in Figure 9. This figure compares two different probabilities, the probability of a sightline having a mock absorber or the probability of a sightline having a total integrated column density above the threshold. Probability is shown as a function of impact parameter.

We can see in Figure 9 that the average probability of a mock sightline containing an O VI absorber is smaller than the probability of the total integrated column density exceeding the threshold at all impact parameters. This suggests that the smaller, cumulative amount of O VI-bearing gas makes significant contributions when integrating along the entire line of sight. This diffuse gas throughout the CGM contributes along much of the sightline. This makes observations complicated as diffuse gas throughout the CGM creates a wide absorption feature due to Doppler broadening as discussed in Section 5.1. Therefore, we expect that observations of O VI lines would be broad. We do see observational evidence that this is true in O VI spectral features (in, e.g., Werk et al. 2016).

The effects of diffuse Mg II are much smaller as the probability distributions in Figure 9 are much closer. Therefore, we expect only a small fraction of sightlines to have diffuse Mg II that would give an observable integrated column density without producing an absorber. This means in a population of mock sightlines Mg II-bearing gas is more effectively modeled as absorption

features, with only smaller contributions from diffuse components.

5.4. Caveats

The analyses in this paper are subject to a variety of challenges and limitations. These include:

1. The simulations themselves implement a specific mode of galaxy formation and the choice of physics for these simulations can affect the structure of the CGM. The FOGGIE simulations do not necessarily implement all possible physics and lack prescriptions for magnetic fields and cosmic rays, which may affect the structure of the CGM for these simulated galaxies (van de Voort et al. 2021; Weber et al. 2025; Butsky et al. 2022). This is also true for our choice of physics in post-processing; for example, the UV background (we use Haardt & Madau 2012) has been shown to greatly affect the resulting ionic column densities in post processing (Taira et al. 2025). The effects of these physics choices are studied by the AGORA Collaboration, and a synthesis of these effects on the CGM can be found in Strawn et al. (2024). Since this paper heavily relies on these ionic column densities, it is important to note that this is a model-dependent quantity.
2. Additionally, we are working with a limited sample size of six galaxy halos and in a very specific mass

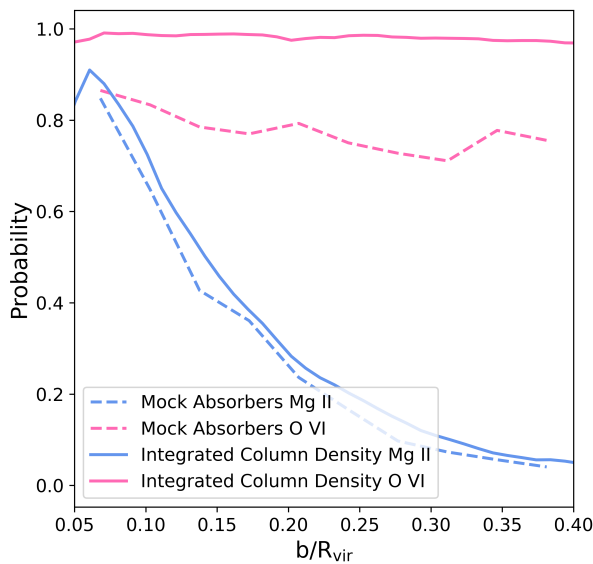


Figure 9. Comparison of the probability of detection for our two different analysis methods, the two-dimensional mock sightlines grids and the the one-dimensional SALSA mock absorber analysis. The solid lines above represent the two-dimensional integrated mock sightline analysis and the dashed lines represent the SALSA mock absorber analysis. The probability of the two-dimensional datasets represents the probability of the total integrated column density being larger than $N = 10^{12.5} \text{ cm}^{-2}$ whereas the probability for the SALSA rays represents whether SALSA finds a spatially and kinematically contiguous absorbers above $N = 10^{12.5} \text{ cm}^{-2}$ along the sightline. The blue lines represent the probability of detecting a Mg II structure for each analysis and the pink lines are the probability of detecting a O VI structure for each analysis. Each line is an average across all of the FOGGIE halos at $z = 0$.

regime ($M_{\text{vir}} \approx (0.50 - 1.5) \times 10^{12} M_{\odot}$) at $z = 0$. These factors both affect the scalability of our study and whether these trends should apply to galaxies more widely.

3. We define a set ion column density threshold of $N = 10^{12.5} \text{ cm}^{-2}$ in Section 3 to denote observable Mg II and O VI column densities. This is only an approximation of the observational column density threshold for these ions, and real observations have numerous factors that affect observability, including observation duration, spectral resolution, signal-to-noise, etc.
4. We can see in Figure 3 that most of the lines of sight have O VI column densities close to the threshold. The consequence of this distribution is that if we increased or decreased our threshold

this would change the probabilities that are shown in Figures 3 and 4. However, even if the quantitative behavior would change the qualitative behavior described throughout this paper would not change significantly.

5. There are multiple parameters that go into the SALSA algorithm that identify individual absorption features that we see in Section 4. We outline in Appendix A what these parameters are and the values we use for this analysis. We note that reasonable changes in these parameters would not have a significant effect on this analysis.
6. We have compared two ways of estimating column densities of individual ions — projected column densities through the entire CGM and an algorithm that identifies individual physically-contiguous structures along a line of sight. Both are approximations of actual astronomical observations in the sense that they lack direct information about the detailed absorption features that may emerge (e.g., line blending from physically distinct features that absorb light at similar wavelengths). More work on the relationship between mock observations and real observations can be found in Marra et al. (2021, 2023). A more realistic method of identifying and relating low- and high-ion gas would be to create and analyze synthetic absorption spectra and analyze them as if they were real astronomical spectra (which is possible using the Trident code). We have chosen not to do so for this project, but rather use a method that focuses on physical structures in galactic systems. We have done our analysis this way as there is uncertainty in tying spectral features to underlying gas and this work was focused on looking at the underlying gas structures.

6. SUMMARY

We have used the FOGGIE simulations to probe the relationship between Mg II and O VI as tracers for low and high ions, or cool and warm gas, respectively. These Milky Way-like galaxy simulations are constructed to have high spatial resolution far out into the simulations' circumgalactic medium, which allows us to effectively probe gas features out to significant fractions of the virial radius.

The key results from this work are as follows:

1. There is an extended halo of O VI that yields column densities greater than $N = 10^{12.5} \text{ cm}^{-2}$ out to impact parameters that are a significant fraction of the virial radius. In contrast, Mg II has a

radial profile that rapidly falls below this column density threshold, meaning that most detectable amounts of Mg II are located close to the galactic disk in all systems that we examined and over a wide range of observable redshifts.

2. Two-dimensional projected mock sightlines show that for low impact parameters we would expect to have both Mg II and O VI at column densities exceeding $N = 10^{12.5} \text{ cm}^{-2}$ in our lines of sight, but above roughly $0.3 - 0.5R_{\text{vir}}$ we expect this to change to sightlines having only detectable amount of O VI.
3. The SALSA one-dimensional ray analysis finds individual physically contiguous structures in a given ion along the mock line of sight. This analysis shows notably lower rates of O VI detection than the two-dimensional projected sightline analysis. This reinforces the idea that O VI-bearing gas exists as a diffuse and extended halo around the galaxy and is not easily classified into single physically over-dense features.
4. We find that Mg II and O VI absorbers appear to be kinematically correlated only when looking at the absorbers with the closest line-of-sight velocities along a sightline. However, this does not correspond to any physical spatial correlation of these mock absorbers and therefore there is no actual co-movement of the gas that traces these ions.
5. Overall the trends in this work are strikingly consistent across redshift and across simulated galaxies. There is some scatter across the six FOGGIE halos, but most plots have remarkable agreement for the six different galaxies. Evolution in redshift is very slight and does not significantly affect any of the trends presented in this paper.

Overall, more work needs to be done to understand the relationship between the cooler gas that is found at small fractions of the virial radius and the diffuse warm medium that surrounds it. Probing the relationship between these states and the interfaces between the cool and warm gas of the circumgalactic medium is key to broadening our understanding of gas dynamics in galaxies.

MT acknowledges support from Michigan State University through the University Distinguished Fellowship program and from the National Science Foundation through the Graduate Research Fellowship Program grant number #2235783. BWO acknowledges support from NSF grants #1908109 and #2106575, NASA ATP grants 80NSSC18K1105 and 80NSSC24K0772, and NASA TCAN grant 80NSSC21K1053. CL was supported by NASA through the NASA Hubble Fellowship grant #HST-HF2-51538.001-A awarded by the Space Telescope Science Institute, which is operated by the Association of Universities for Research in Astronomy, Inc., for NASA, under contract NAS5-26555. CWT was supported for this work in part by NASA via a Theoretical and Computational Astrophysics Networks grant #80NSSC21K1053 and JWST AR #5486. RA acknowledges funding from the European Research Council (ERC) under the European Union’s Horizon 2020 research and innovation programme (grant agreement 101020943, SPECMAP-CGM).

Computational resources supporting this work were provided by the NASA High-End Computing (HEC) Program through the NASA Advanced Supercomputing (NAS) Division at Ames Research Center and were sponsored by NASA’s Science Mission Directorate; we are grateful for the superb user-support provided by NAS. Resources were also provided by the Blue Waters sustained-petascale computing project, which is supported by the NSF (award numbers ACI-1238993 and ACI-1514580) and the state of Illinois. This work also used the resources of the Michigan State University High Performance Computing Center, operated by the MSU Institute for Cyber-Enabled Research. Simulations described in this work were performed using the publicly-available Enzo code, which is the product of a collaborative effort of many independent scientists from numerous institutions around the world.

M. T. contributed conceptualization, investigation, formal analysis, visualization, writing (original draft). B. W. O. contributed to conception, supervision, writing (review and editing). C. K. contributed to software, methodology, and writing (review and editing). C. L. contributed to conceptualization and writing (review and editing). M. P. contributed conceptualization and writing (review and editing). J. T. contributed conceptualization and writing (review and editing). C. T. contributed conceptualization and writing (review and editing). V. S. contributed conceptualization. R. A. contributed conceptualization and writing (review and editing) N. L. contributed conceptualization and writing (review and editing). B. D. S. contributed concep-

tualization and writing (review and editing). J. C. H. contributed conceptualization and writing (review and editing).

Software: Enzo (Bryan et al. 2014; Brummel-Smith et al. 2019), yt (Turk et al. 2011), Trident (Hummels et al. 2017), SALSA (Boyd et al. 2020), MATPLOTLIB (Hunter 2007), NUMPY (Walt et al. 2011), SCIPY (Virtanen et al. 2020), astropy (Astropy Collaboration et al. 2013, 2018), ChatGPT (OpenAI 2025), Claude (Anthropic 2025).

REFERENCES

Anthropic. 2025, Claude (Opus family), <https://www.anthropic.com/>

Astropy Collaboration, Robitaille, T. P., Tollerud, E. J., et al. 2013, *A&A*, 558, A33, doi: [10.1051/0004-6361/201322068](https://doi.org/10.1051/0004-6361/201322068)

Astropy Collaboration, Price-Whelan, A. M., Sipőcz, B. M., et al. 2018, *AJ*, 156, 123, doi: [10.3847/1538-3881/aabc4f](https://doi.org/10.3847/1538-3881/aabc4f)

Boyd, B. I., Silvia, D. W., O’Shea, B. W., et al. 2020, *Journal of Open Source Software*, 5, 2581, doi: [10.21105/joss.02581](https://doi.org/10.21105/joss.02581)

Brummel-Smith, C., Bryan, G., Butsky, I., et al. 2019, *Journal of Open Source Software*, 4, 1636, doi: [10.21105/joss.01636](https://doi.org/10.21105/joss.01636)

Bryan, G. L., Norman, M. L., O’Shea, B. W., et al. 2014, *The Astrophysical Journal Supplement Series*, 211, 19, doi: [10.1088/0067-0049/211/2/19](https://doi.org/10.1088/0067-0049/211/2/19)

Butsky, I. S., Werk, J. K., Tchernyshyov, K., et al. 2022, *The Astrophysical Journal*, 935, 69, doi: [10.3847/1538-4357/ac7ebd](https://doi.org/10.3847/1538-4357/ac7ebd)

Cen, R., & Ostriker, J. P. 1992, *The Astrophysical Journal*, 399, L113, doi: [10.1086/186620](https://doi.org/10.1086/186620)

—. 2006, *The Astrophysical Journal*, 650, 560, doi: [10.1086/506505](https://doi.org/10.1086/506505)

Chen, H.-W., Wild, V., Tinker, J. L., et al. 2010, *The Astrophysical Journal*, 724, L176, doi: [10.1088/2041-8205/724/2/L176](https://doi.org/10.1088/2041-8205/724/2/L176)

Chen, Z., Wang, E., Zou, H., et al. 2025, *The Astrophysical Journal*, 981, 81, doi: [10.3847/1538-4357/ada942](https://doi.org/10.3847/1538-4357/ada942)

Cherrey, M., Bouché, N. F., Zabl, J., et al. 2025, *Astronomy & Astrophysics*, 694, A117, doi: [10.1051/0004-6361/202451165](https://doi.org/10.1051/0004-6361/202451165)

Corlies, L., Peebles, M. S., Tumlinson, J., et al. 2020, *The Astrophysical Journal*, 896, 125, doi: [10.3847/1538-4357/ab9310](https://doi.org/10.3847/1538-4357/ab9310)

Dutta, S., Muzahid, S., Schaye, J., et al. 2025, *The Astrophysical Journal*, 985, 44, doi: [10.3847/1538-4357/adc922](https://doi.org/10.3847/1538-4357/adc922)

Emerick, A., Bryan, G. L., & Mac Low, M.-M. 2019, *Monthly Notices of the Royal Astronomical Society*, 482, 1304, doi: [10.1093/mnras/sty2689](https://doi.org/10.1093/mnras/sty2689)

Ferland, G. J., Porter, R. L., van Hoof, P. A. M., et al. 2013, *RMxAA*, 49, 137, doi: [10.48550/arXiv.1302.4485](https://doi.org/10.48550/arXiv.1302.4485)

Fox, A. J., Frazer, E. M., Bland-Hawthorn, J., et al. 2020, *The Astrophysical Journal*, 897, 23, doi: [10.3847/1538-4357/ab92a3](https://doi.org/10.3847/1538-4357/ab92a3)

Haardt, F., & Madau, P. 2012, *The Astrophysical Journal*, 746, 125, doi: [10.1088/0004-637X/746/2/125](https://doi.org/10.1088/0004-637X/746/2/125)

Helmi, A., Babusiaux, C., Koppelman, H. H., et al. 2018, *Nature*, 563, 85, doi: [10.1038/s41586-018-0625-x](https://doi.org/10.1038/s41586-018-0625-x)

Ho, S. H., Martin, C. L., Nataf, H., Kacprzak, G. G., & Stern, J. 2025, Kinematics of Circumgalactic O VI Gas and Disk Rotation of ≈ 0.2 Star-forming Galaxies, arXiv, doi: [10.48550/arXiv.2507.11664](https://doi.org/10.48550/arXiv.2507.11664)

Hummels, C. B., Smith, B. D., & Silvia, D. W. 2017, *ApJ*, 847, 59, doi: [10.3847/1538-4357/aa7e2d](https://doi.org/10.3847/1538-4357/aa7e2d)

Hummels, C. B., Smith, B. D., Hopkins, P. F., et al. 2019, *The Astrophysical Journal*, 882, 156, doi: [10.3847/1538-4357/ab378f](https://doi.org/10.3847/1538-4357/ab378f)

Hunter, J. D. 2007, Computing in Science and Engineering, 9, 90, doi: [10.1109/MCSE.2007.55](https://doi.org/10.1109/MCSE.2007.55)

Lehner, N., Howk, J. C., & Wakker, B. P. 2015, *The Astrophysical Journal*, 804, 22, doi: [10.1088/0004-637X/804/2/79](https://doi.org/10.1088/0004-637X/804/2/79)

Lehner, N., O’Meara, J. M., Fox, A. J., et al. 2014, *The Astrophysical Journal*, 788, 119, doi: [10.1088/0004-637X/788/2/119](https://doi.org/10.1088/0004-637X/788/2/119)

Lehner, N., Berek, S. C., Howk, J. C., et al. 2020, *The Astrophysical Journal*, 900, 9, doi: [10.3847/1538-4357/aba49c](https://doi.org/10.3847/1538-4357/aba49c)

Lehner, N., Kopenhafer, C., O’Meara, J. M., et al. 2022, *The Astrophysical Journal*, 936, 156, doi: [10.3847/1538-4357/ac7400](https://doi.org/10.3847/1538-4357/ac7400)

Lehner, N., Howk, J. C., Collins, L., et al. 2025, Project AMIGA: The Inner Circumgalactic Medium of Andromeda from Thick Disk to Halo, arXiv, doi: [10.48550/arXiv.2506.16573](https://doi.org/10.48550/arXiv.2506.16573)

Marra, R., Churchill, C. W., Kacprzak, G. G., et al. 2023, *Monthly Notices of the Royal Astronomical Society*, 527, 10522, doi: [10.1093/mnras/stad3735](https://doi.org/10.1093/mnras/stad3735)

Marra, R., Churchill, C. W., Doughty, C., et al. 2021, *Monthly Notices of the Royal Astronomical Society*, 508, 4938, doi: [10.1093/mnras/stab2896](https://doi.org/10.1093/mnras/stab2896)

OpenAI. 2025, ChatGPT, <https://chat.openai.com/>

Peeples, M. S., Corlies, L., Tumlinson, J., et al. 2019, *The Astrophysical Journal*, 873, 129, doi: [10.3847/1538-4357/ab0654](https://doi.org/10.3847/1538-4357/ab0654)

Péroux, C., & Howk, J. C. 2020, *Annual Review of Astronomy and Astrophysics*, 58, 363, doi: [10.1146/annurev-astro-021820-120014](https://doi.org/10.1146/annurev-astro-021820-120014)

Qu, Z., Pan, Z., Bregman, J. N., & Liu, J. 2024, *ApJ*, 965, 100, doi: [10.3847/1538-4357/ad31a0](https://doi.org/10.3847/1538-4357/ad31a0)

Qu, Z., Chen, H.-W., Johnson, S. D., et al. 2024, *The Astrophysical Journal*, 968, 8, doi: [10.3847/1538-4357/ad410b](https://doi.org/10.3847/1538-4357/ad410b)

Sameer, Lehner, N., Howk, J. C., et al. 2024, The COS CGM Compendium V: The Dichotomy of OVI Associated with Low- and High-Metallicity Cool Gas at $z < 1$, arXiv, doi: [10.48550/arXiv.2403.02374](https://doi.org/10.48550/arXiv.2403.02374)

Simons, R. C., Peeples, M. S., Tumlinson, J., et al. 2020, *The Astrophysical Journal*, 905, 167, doi: [10.3847/1538-4357/abc5b8](https://doi.org/10.3847/1538-4357/abc5b8)

Smith, B. D., Hallman, E. J., Shull, J. M., & O'Shea, B. W. 2011, *The Astrophysical Journal*, 731, 6, doi: [10.1088/0004-637X/731/1/6](https://doi.org/10.1088/0004-637X/731/1/6)

Smith, B. D., Bryan, G. L., Glover, S. C. O., et al. 2017, *Monthly Notices of the Royal Astronomical Society*, 466, 2217, doi: [10.1093/mnras/stw3291](https://doi.org/10.1093/mnras/stw3291)

Stocke, J. T., Keeney, B. A., Danforth, C. W., et al. 2013, *The Astrophysical Journal*, 763, 148, doi: [10.1088/0004-637X/763/2/148](https://doi.org/10.1088/0004-637X/763/2/148)

Strawn, C., Roca-Fàbrega, S., Primack, J. R., et al. 2024, *The Astrophysical Journal*, 962, 29, doi: [10.3847/1538-4357/ad12cb](https://doi.org/10.3847/1538-4357/ad12cb)

Suresh, J., Nelson, D., Genel, S., Rubin, K. H. R., & Hernquist, L. 2019, *Monthly Notices of the Royal Astronomical Society*, 483, 4040, doi: [10.1093/mnras/sty3402](https://doi.org/10.1093/mnras/sty3402)

Taira, E., Kopenhafer, C., O'Shea, B. W., et al. 2025, *The Astrophysical Journal*, 991, 221, doi: [10.3847/1538-4357/adfc4e](https://doi.org/10.3847/1538-4357/adfc4e)

Tripp, T. M., Sembach, K. R., Bowen, D. V., et al. 2008, *The Astrophysical Journal Supplement Series*, 177, 39, doi: [10.1086/587486](https://doi.org/10.1086/587486)

Tumlinson, J., Peeples, M. S., & Werk, J. K. 2017, *Annual Review of Astronomy and Astrophysics*, 55, 389, doi: [10.1146/annurev-astro-091916-055240](https://doi.org/10.1146/annurev-astro-091916-055240)

Turk, M. J., Smith, B. D., Oishi, J. S., et al. 2011, *The Astrophysical Journal Supplement Series*, 192, 9, doi: [10.1088/0067-0049/192/1/9](https://doi.org/10.1088/0067-0049/192/1/9)

van de Voort, F., Bieri, R., Pakmor, R., et al. 2021, *Monthly Notices of the Royal Astronomical Society*, 501, 4888, doi: [10.1093/mnras/staa3938](https://doi.org/10.1093/mnras/staa3938)

van de Voort, F., Springel, V., Mandelker, N., van den Bosch, F. C., & Pakmor, R. 2019, *Monthly Notices of the Royal Astronomical Society: Letters*, 482, L85, doi: [10.1093/mnrasl/sly190](https://doi.org/10.1093/mnrasl/sly190)

Virtanen, P., Gommers, R., Oliphant, T. E., et al. 2020, *Nature Methods*, 17, 261, doi: [10.1038/s41592-019-0686-2](https://doi.org/10.1038/s41592-019-0686-2)

Walt, S. v. d., Colbert, S. C., & Varoquaux, G. 2011, *Computing in Science & Engineering*, 13, 22

Weber, M., Thomas, T., Pfrommer, C., & Pakmor, R. 2025, *Astronomy & Astrophysics*, 698, A125, doi: [10.1051/0004-6361/202553954](https://doi.org/10.1051/0004-6361/202553954)

Werk, J. K., Prochaska, J. X., Tumlinson, J., et al. 2014, *The Astrophysical Journal*, 792, 8, doi: [10.1088/0004-637X/792/1/8](https://doi.org/10.1088/0004-637X/792/1/8)

Werk, J. K., Prochaska, J. X., Cantalupo, S., et al. 2016, *The Astrophysical Journal*, 833, 54, doi: [10.3847/1538-4357/833/1/54](https://doi.org/10.3847/1538-4357/833/1/54)

Wright, A. C., Tumlinson, J., Peeples, M. S., et al. 2024, *The Astrophysical Journal*

APPENDIX

A. ABSORPTION IDENTIFICATION METHODS IN SALSA

SALSA uses an iterative method to identify absorbers along a line of sight. First, it finds the total ion column density along a line of sight. Then, it sets a threshold at 80% of the total column density and then identifies the continuous segments of gas that lie above this threshold. Next, SALSA masks out the regions that have already been identified. It then again set a line at 80% of the column density of the remaining gas and identify the continuous segments of gas that lie above the threshold. Then it checks if any newly identified absorbers can be combined with absorbers from the previous steps by checking if they connect spatially and the average line-of-sight velocities have a difference of less than 10 km/s. It iteratively performs these steps again until the total column density of the species in question that is not contained within an absorber drops below $N = 10^{12.5} \text{ cm}^{-2}$ (which is typically a very small fraction of the total line-of-sight column density). Finally, SALSA checks to see if all of the absorbers identified reach the minimum observable value, which is the same threshold that terminates the iteration process — $N = 10^{12.5} \text{ cm}^{-2}$.

The 80% column density threshold, the velocity threshold (10 km/s), and the minimum column density threshold $N = 10^{12.5} \text{ cm}^{-2}$ are all parameters that are set by the algorithm and can be changed by the user. We choose to use the default parameters for the 80% column density threshold and the velocity threshold. We change the minimum column density from its default value of $N = 10^{13} \text{ cm}^{-2}$ to $N = 10^{12.5} \text{ cm}^{-2}$ to match the other analysis in the paper.